Importance of force decomposition for local stress calculations in biomembrane molecular simulations

Juan M. Vanegas,[†,‡] Alejandro Torres-Sánchez,[†,‡] and Marino Arroyo[*,†]

LaCàN, Universitat Politècnica de Catalunya-BarcelonaTech, Barcelona, Spain

E-mail: marino.arroyo@upc.edu

Abstract

Local stress fields are routinely computed from molecular dynamics trajectories to understand the structure and mechanical properties of lipid bilayers. These calculations can be systematically understood with the Irving-Kirkwood-Noll theory. In identifying the stress tensor, a crucial step is the decomposition of the forces on the particles into pairwise contributions. However, such a decomposition is not unique in general, leading to an ambiguity in the definition of the stress tensor, particularly for multibody potentials. Furthermore, a theoretical treatment of constraints in local stress calculations has been lacking. Here, we present a new implementation of local stress calculations that systematically treats constraints and considers a privileged decomposition, the central force decomposition, that leads to a symmetric stress tensor by construction. We focus on biomembranes, although the methodology presented here is widely applicable. Our results show that some unphysical behavior obtained with previous implementations, e.g. non-constant normal stress profiles along an isotropic bilayer in equilibrium, is a consequence of an improper treatment of constraints. Furthermore, other valid force decompositions produce significantly different stress profiles, particularly in the presence of

---

[*]To whom correspondence should be addressed
[†]Universitat Politècnica de Catalunya-BarcelonaTech
[‡]Contributed equally to this work

dihedral potentials. Our methodology reveals the striking effect of unsaturations on the bilayer mechanics, missed by previous stress calculation implementations.

Introduction

Lipid membranes compartmentalize and spatially segregate the numerous processes that take place within the cell. These membranes are composed of a variety of lipid species such as phospholipids and sterols, and they also host a large number of associated and integral membrane proteins. Many of the lipids in the membrane are involved in the regulation of biological functions through specific biochemical interactions,[1–3] yet the structure (e.g. bilayer thickness) and mechanics (e.g. bending modulus) of the membrane also play an important, and in many cases critical, role in the function of bilayers and associated proteins involved in processes such as mechanotransduction, signaling, and transport.[4–8] While some bulk mechanical properties of the membrane can readily be obtained experimentally or computationally, such as the area compressibility or the bending elastic moduli, other important mechanical features, such as the stress state within the bilayer or in the vicinity of an inclusion, are not easily accessible. Furthermore, it is not clear how to relate mesoscopic properties with atomic and molecular interactions.

Statistical mechanics bridges these different scales and provides a local definition of the stress tensor, $\sigma(x)$, from the interaction forces and velocities of individual atoms. This idea was first introduced by Irving and Kirkwood in a landmark paper,[9] and later developed by Noll[10] and others.[11–15] For fluid isotropic membranes, σ reduces to two components conventionally defined as $P_L = -\left(\sigma_{xx} + \sigma_{yy}\right)/2$ (in the plane $x - y$ of the membrane), and $P_N = -\sigma_{zz}$ (normal to the membrane), both of which only depend on the position along the bilayer normal, z. For bilayers in mechanical equilibrium, P_N must be constant in the system. With these two components of the stress, we can further define the lateral pressure profile $\pi(z) = P_L(z) - P_N(z)$. This quantity exemplifies the connection between molecular simulations and continuum theories, as its first and second moments result in the bending modulus times the spontaneous curvature and minus

the Gaussian modulus respectively.[16] It has been hypothesized that the function of membrane proteins can be directly modulated by changes in the stress profile.[16,17] The lateral pressure is also frequently used to assess whether coarse-grained models reproduce the mechanical properties of atomistic systems.[18–20] Obtaining experimental measurements of the local stress within a membrane is very challenging, with few studies that have used fluorescent probes to measure changes in the internal stress.[21,22]

Molecular dynamics (MD) simulations are increasingly being used to evaluate the stress tensor in lipid bilayers from atomistic[23–30] and coarse-grained[19,20,27,30–32] models. To calculate the local stress from MD, the pointwise expressions resulting from the Irving and Kirkwood theory are spatially averaged.[11,12] While simulations of coarse-grained membranes show constant P_N profiles, several atomistic studies[26,29,30] have obtained non-constant P_N values for isotropic bilayers at equilibrium. It has been suggested[30,33–36] that this unphysical result arises from bond constraints, since coarse-grained simulations treat bonds with harmonic potentials. This issue is further complicated by the fact that many works in the field do not report P_L and P_N separately.

A fundamental step in the Irving-Kirkwood-Noll (IKN) theory for local stress calculations is the decomposition of the forces acting on particles into pairwise contributions that satisfy the weak law of action-reaction. For pair potentials, there is a canonical pairwise decomposition.[9] Furthermore, this decomposition is central, i.e. each pairwise force is aligned with the vector connecting the pair of particles. However, force decompositions are not unique in general, and there is not a clear notion of canonical decomposition for multibody potentials. Different decompositions lead to different local stresses, which differ by a divergence-free field.[15,37] Specific force decompositions of multibody interactions have been proposed in the context of biomembrane simulations,[14] which are not central and may lead to non-symmetric stress tensors.[15] In contrast, it has been recently shown that central force decompositions always exist, and provide stress tensors that satisfy the balance of angular momentum.[15,37] Another aspect that has brought confusion in the field is the treatment of constraints, very common in molecular simulations, since these are not addressed in theories of local stress,[9,14,15] but are included in MD implementations of local stress calcula-

tions.[32,38]

Here, we note that for potentials with up to four-body interactions, such as those used in biomolecular simulations, there is a natural and unambiguous notion of central force decomposition. Furthermore, since the Liouville equation remains essentially unchanged in the presence of constraints,[39] we argue that constraint forces admit a straightforward treatment within the IKN theory. We implement the resulting method within the Gromacs[40] MD simulation package, make it publicly available,[41] and exercise it on different coarse-grained and atomistic models of lipid bilayers. In addition to the central force decomposition, we also include in our software implementation a previously proposed force decomposition of multibody potentials,[14] and show that it produces significantly different stress profiles in atomistic systems. By comparing our results with a popular implementation of stress calculation in biomolecular simulations,[42] we highlight the importance of a consistent treatment of the constraints. Furthermore, we show that the proper decomposition of forces enables the exploration of new and surprising features in the mechanical properties of membranes, such as the large contribution of double bonds to the overall stress profile.

Theory

General theory of the local stress

The idea of obtaining pointwise continuum fields from the positions and velocities of individual particles, as defined by expectation values from non-equilibrium classical statistical mechanics, was pioneered by Irving and Kirkwood.[9] This theory was more rigorously developed by Noll,[10] resulting in the so-called Irving-Kirkwood-Noll (IKN) procedure. Due to both the statistical and the pointwise nature of the fields in the IKN procedure, calculating them from atomistic simulations requires that every point within the volume of the system be well sampled, which is practically unfeasible. This difficulty was independently overcome by Hardy et al.[11,43] and Murdoch[12,44,45] through the definition of new continuum fields as spatial averages of the pointwise IKN fields. Similar ideas can also be found in the work of Schofield and Henderson.[13]

Despite this long history, the theory of local stress calculations from atomistic models is not fully settled, particularly for multibody potentials. To appreciate this fact, let us briefly outline part of the IKN procedure. A key step to identify the potential component of the stress tensor before spatial averaging, $\sigma^{\mathrm{pt},V}$, is expressing the right-hand side of the equation

$$\operatorname{div} \sigma^{\mathrm{pt},V}(\boldsymbol{x}) = \sum_{\alpha} \langle \boldsymbol{F}^{\alpha} \delta(\boldsymbol{r}^{\alpha} - \boldsymbol{x}) \rangle \tag{1}$$

in divergence form. Here, $\boldsymbol{F}^{\alpha}$ is the total force acting on particle α, δ refers to the Dirac-delta distribution, and $\langle \cdot \rangle$ denotes statistical expectation. For pair-potentials, there is a canonical decomposition of the forces acting on particles as

$$\boldsymbol{F}^{\alpha} = \sum_{\beta(\neq\alpha)} \frac{\partial V^{\alpha\beta}}{\partial \boldsymbol{r}^{\alpha}} = -\sum_{\beta(\neq\alpha)} \frac{\partial V^{\alpha\beta}}{\partial \boldsymbol{r}^{\beta}} = \sum_{\beta(\neq\alpha)} \boldsymbol{f}^{\alpha\beta} \tag{2}$$

where the pair potential $V^{\alpha\beta}$ depends on $\boldsymbol{r}^{\alpha}$ and $\boldsymbol{r}^{\beta}$ through the distance between the two particles, $r^{\alpha\beta}$. Consequently,

[A] $\boldsymbol{f}^{\alpha\beta} = -\boldsymbol{f}^{\beta\alpha}$,

[B] $\boldsymbol{f}^{\alpha\beta}$ is parallel to $\boldsymbol{r}^{\alpha\beta} = \boldsymbol{r}^{\beta} - \boldsymbol{r}^{\alpha}$.

From the antisymmetry property [A], one can resort to results by Noll[10,37] and express the right-hand side of Eq. (1) in divergence form involving straight integration paths. Furthermore, from property [B], the resulting stress tensor is symmetric, thereby satisfying the balance of angular momentum of a simple continuum medium.

In MD simulations at equilibrium, the IKN pointwise stress can be evaluated from time aver-

ages and further averaged spatially, resulting in the so-called Hardy stress tensor

$$\boldsymbol{\sigma}(\boldsymbol{x}) = \boldsymbol{\sigma}^K(\boldsymbol{x}) + \boldsymbol{\sigma}^V(\boldsymbol{x}),$$

$$\boldsymbol{\sigma}^K(\boldsymbol{x}) = -\frac{1}{N_T} \sum_{i=1}^{N_T} \left[\sum_\alpha m^\alpha w \left(\boldsymbol{x}; r_i^\alpha - \boldsymbol{x} \right) \, \boldsymbol{v}_i^\alpha \otimes \boldsymbol{v}_i^\alpha \right],$$

$$\boldsymbol{\sigma}^V(\boldsymbol{x}) = \frac{1}{2N_T} \sum_{i=1}^{N_T} \left[\sum_{\alpha,\beta(\neq\alpha)} r_i^{\alpha\beta} \otimes f_i^{\alpha\beta} \, B \left(\boldsymbol{x}; r_i^\alpha, r_i^\beta \right) \right],$$

(3)

where m^α, r_i^α, v_i^α and $f_i^{\alpha\beta}$ are the masses, positions, velocities, and pairwise forces at time-step i, and N_T is the total number of time-steps. The symbol $\otimes$ denotes the dyadic product, e.g. $v_i^\alpha \otimes v_i^\alpha$ is a second-order tensor. The stress has a kinetic contribution, $\boldsymbol{\sigma}^K(\boldsymbol{x})$, that stems from the flux of momentum associated with the vibrational internal energy of the system, and a potential contribution, $\boldsymbol{\sigma}^V(\boldsymbol{x})$, which accounts for the internal forces between particles.[15,37] From the expression for $\boldsymbol{\sigma}^V$, it is clear that property [B] implies symmetry of the stress tensor. The spatial averaging of these two quantities is performed by the function $w(\boldsymbol{x}; \boldsymbol{y})$ supported in a domain $\Omega_{\boldsymbol{x}}$ centered at $\boldsymbol{x}$, which weights the contribution to the stress from the particles located at $\boldsymbol{y}$ in $\Omega_{\boldsymbol{x}}$. This weighting function must be normalized, i.e. $\int_{\Omega_{\boldsymbol{x}}} d\boldsymbol{y} \, w(\boldsymbol{x}; \boldsymbol{y}) = 1$. To evaluate $\boldsymbol{\sigma}^V(\boldsymbol{x})$, the weight function must be integrated over the line segment connecting particles α and β to account for their interaction, which results in the bond function $B \left(\boldsymbol{x}; r_i^\alpha, r_i^\beta \right) = \int_{s=0}^1 ds \, w \left(\boldsymbol{x}; (1-s)r_i^\alpha + sr_i^\beta \right)$. The potential part of the stress $\boldsymbol{\sigma}^V(\boldsymbol{x})$ can be interpreted as a time and space average of the interactions crossing $\Omega_{\boldsymbol{x}}$.

In the limit of uniform weight over the entire volume of the system V, and noting that $\sum_{\alpha,\beta(\neq\alpha)} f^{\alpha\beta} \otimes r^{\alpha\beta} = -2 \sum_\alpha \boldsymbol{F}^\alpha \otimes \boldsymbol{r}^\alpha$, the Hardy stress takes the form of the virial stress

$$\boldsymbol{\sigma}^T = -\frac{1}{N_T} \sum_{i=1}^{N_T} \frac{1}{V} \left[\sum_\alpha m^\alpha \boldsymbol{v}^\alpha \otimes \boldsymbol{v}^\alpha + \boldsymbol{F}^\alpha \otimes \boldsymbol{r}^\alpha \right],$$

(4)

which is typically used in MD simulations to measure the total pressure of the system.

Local stress and multibody potentials

For multibody potentials, the notion of canonical force decomposition is not so clear. It can be shown that it is always possible to decompose $\boldsymbol{F}^\alpha = \sum_{\beta(\neq\alpha)} \boldsymbol{f}^{\alpha\beta}$ such that properties [A] and [B] are satisfied, which is referred to as a central force decomposition (CFD).[15] Then, Noll's procedure can be carried out and the resulting stress tensor, which also follows from Eq. (3), is symmetric. In a CFD, we have

$$\boldsymbol{F}^\alpha = \sum_{\beta(\neq\alpha)} \boldsymbol{f}^{\alpha\beta} = \sum_{\beta(\neq\alpha)} \varphi^{\alpha\beta} \frac{\boldsymbol{r}^{\alpha\beta}}{r^{\alpha\beta}}, \tag{5}$$

where $\left|\varphi^{\alpha\beta}\right|$ is the magnitude of the force between α and β and sign $\left(\varphi^{\alpha\beta}\right) = \pm 1$ indicates whether the force is repulsive (-1) or attractive $(+1)$. A CFD can be theoretically defined as follows. Due to the translational and rotational invariance of classical mechanics, any interatomic potential, $V(\{\boldsymbol{r}^\alpha\})$, must only depend on the relative distances between the particles of the system, i.e. there exists a function $\widetilde{V}\left(\{r^{\alpha\beta}\}\right)$ depending on the distances between particles such that $V(\{\boldsymbol{r}^\alpha\}) = \widetilde{V}\left(\{r^{\alpha\beta}\}\right)$. Under mild technical conditions on $\widetilde{V}\left(\{r^{\alpha\beta}\}\right)$, generally satisfied for the potentials in MD simulations, a CFD follows from[15,37]

$$\varphi^{\alpha\beta} = \frac{\partial \widetilde{V}\left(\{r^{\alpha\beta}\}\right)}{\partial r^{\alpha\beta}}. \tag{6}$$

Since the representation $\widetilde{V}$ is not unique, the CFD is not unique either. This fact can be appreciated by counting equations and unknowns. For a multibody interaction involving $N \geq 3$ particles, the independent components of the forces (N forces satisfying conservation of linear and angular momenta) lead to $3N - 6$ equations. On the other hand, the number of pairwise central terms is $N(N-1)/2$. Although in general we have more unknowns than equations, for $N = 3$ or $N = 4$, the number of equations and unknowns coincide, and therefore the CFD is unique. Thus, for potentials with up to four-body interactions, e.g. dihedral potentials, there is a reasonable notion of a canonical CFD, which considers the unique central decomposition of each additive part of the potential separately.

When the CFD is not unique, each decomposition leads to a different stress tensor. Nevertheless, recalling Eq. (1), these stress fields differ by a divergence-free field and $\nabla \cdot \boldsymbol{\sigma}(\boldsymbol{x})$ is uniquely defined. In fact, other authors have proposed force decompositions that are not central. For instance, building on a different re-elaboration of the Irving and Kirkwood theory,[13] Goetz and Lipowsky[14] proposed a method for stress calculation essentially equivalent to Eq. (3) with the decomposition

$$f_{GL}^{\alpha\beta} = \sum_M \frac{1}{n_M} \left(\frac{\partial V_M}{\partial \boldsymbol{r}^\beta} - \frac{\partial V_M}{\partial \boldsymbol{r}^\alpha} \right), \tag{7}$$

where M labels potential contributions V_M (e.g. two-, three-, four-body potentials) involving particles α and β, and n_M denotes the number of particles involved in V_M. While this decomposition, which we refer to as GLD, satisfies property [A], it does not satisfy [B] in general, and therefore may lead to non-symmetric tensor fields.[15] This makes it difficult to interpret such a stress, which we denote as $\boldsymbol{\sigma}^{GL}$, in terms of continuum mechanics of simple bodies. However, as discussed above, $\boldsymbol{\sigma}^{GL}$ and a stress tensor based on a CFD differ by a divergence-free field. For pair potentials, both CFD and GLD recover the IKN theory, i.e. both decompositions result in the same stress tensor.

Treatment of constraints

Bonds in MD simulations are often treated with rigid constraints to increase the integration time-step and improve the computational efficiency. Common constraint algorithms include LINCS,[46] SHAKE,[47] and SETTLE.[48] It has been suggested that the treatment of constraints in stress calculation algorithms is responsible for reported unphysical non-uniform pressures perpendicular to a bilayer in equilibrium,[30,33–36] as further discussed in the next Section. Although previous works[32,33] have suggested implementing bond constraints in the natural way we advocate next, to our knowledge a theoretical justification in the theory of local stress calculations is lacking. Here, we argue that constraints admit a straightforward treatment within the IKN procedure by noting that Liouville's equation, a cornerstone in Irving and Kirkwood's theory, remains essentially un-

changed in the presence of constraints.[39] Considering Q constraints denoted by $C_q(\{r^\alpha\}) = 0$, Liouville's equation governing the evolution of the probability distribution of the system takes the form

$$\frac{\partial f}{\partial t} = \sum_\alpha \left[-v^\alpha \cdot \frac{\partial f}{\partial r^\alpha} + \frac{1}{m^\alpha} \underbrace{\left(\frac{\partial V}{\partial r^\alpha} + \sum_q F_q^\alpha \right)}_{F^\alpha} \cdot \frac{\partial f}{\partial v^\alpha} \right], \tag{8}$$

where $F_q^\alpha = \lambda_q \partial C_q / \partial r^\alpha$ are the constraint forces and λ_q are the corresponding Lagrange multipliers provided by the constraint algorithms. Based on this, the IKN procedure outlined earlier can be directly applied to the constrained system, where F^α includes now the constraint forces. Note that a given particle may be subject to multiple constraints simultaneously, e.g. a carbon atom bonded to four other atoms. Following the common approach of decomposing separately each additive contribution to F^α, and noting that a bond constraint $C_q = r^{\alpha\beta} - d = 0$ between particles α and β depends only on their distance, the corresponding constraint forces admit a trivial decomposition $F_q^\alpha = f_q^{\alpha\beta} = \lambda_q r^{\alpha\beta} / r^{\alpha\beta}$ satisfying [A] and [B].

A recent report[38] has approached the treatment of constraints in stress calculations considering the long-range origin of these interactions. It is argued that, since the constraint force on a pair of particles α and β depends in general on the positions of all other particles interacting with α and β, the GLD,[14] see Eq. (7), suggests that this constraint force should be decomposed into many possibly long-ranged contributions. Given the phenomenal complexity of this procedure, an approximation focusing on Coulomb interactions has been proposed.[38] While this approach may yield a legitimate force decomposition satisfying [A], such a decomposition of bond constraint forces may seem unreasonable from the following perspective. The constrained dynamics can be approximated by replacing bond constraints by harmonic potentials of high stiffness, which in the Irving and Kirkwood procedure lead to individual pair contributions in Eq. (3), as in our treatment of bond constraints. Physically, it is not clear why, when passing to the limit of infinite stiffness, this force should spread into many nonlocal interactions.

Stress in lipid bilayers

The stress tensor provides precise information about the internal forces of the system seen as a continuum. Isolating a sub-domain bounded by an internal surface Γ, the force per unit area exerted by the rest of the system at a point $\boldsymbol{x}$ in Γ, with outward normal $\boldsymbol{n}(\boldsymbol{x})$, can be computed as $\boldsymbol{t}(\boldsymbol{x}) = \boldsymbol{\sigma}(\boldsymbol{x}) \cdot \boldsymbol{n}(\boldsymbol{x})$, referred to as the traction vector. The traction is generally not aligned with $\boldsymbol{n}$. Since by definition the Hardy stress tensor with a CFD decomposition (property [B]) is symmetric, it can be diagonalized in an orthonormal basis. For a transversely isotropic system such as a planar lipid bilayer in water, this basis of eigenvectors is given by any two orthogonal vectors in the plane of the bilayer, e.g. $\boldsymbol{e}_x$ and $\boldsymbol{e}_y$, and a vector normal to it along z, e.g. $\boldsymbol{e}_z$. Along the eigenvectors, the traction is aligned with the normal, e.g. $\boldsymbol{t}_x = \boldsymbol{\sigma}(\boldsymbol{x}) \cdot \boldsymbol{e}_x = \sigma_{xx} \boldsymbol{e}_x$ where σ_{xx} is an eigenvalue of the stress tensor–the principal stress along x. By symmetry of a planar bilayer and for a system in equilibrium, $\sigma_{xx} = \sigma_{yy}$, and the three principal stresses depend only on z. Therefore, the stress tensor is commonly summarized by $P_L(z) = -\left(\sigma_{xx} + \sigma_{yy}\right)/2$, which can be interpreted as the negative of the in-plane traction, and $P_N(z) = -\sigma_{zz}$, the negative of the normal traction. Positive values of these profiles reflect repulsive interactions.

For a system in equilibrium and in the absence of external forces, $\nabla \cdot \boldsymbol{\sigma} = \boldsymbol{0}$. Specializing this equation for a bilayer, we find that $dP_N/dz = 0$, and therefore the normal stress profile should be constant. This physical requirement has been invoked to assess the quality of simulation protocols[49] or stress calculation methods.[50] Its violation in atomistic simulations of lipid bilayers[26,29,30,33] has sparkled some controversy about the role of constraints, as discussed in the previous section.

Although in general the stress tensor stemming from the GLD is not symmetric, when particularized to planar fluid bilayers in equilibrium it is still a diagonal tensor with only z dependence due to the symmetry of the system. As discussed earlier, $\nabla \cdot \left(\boldsymbol{\sigma} - \boldsymbol{\sigma}^{GL}\right) = \boldsymbol{0}$, which implies that $P_N^{GL}(z)$ should be constant, but remarkably does not pose any constraint on $P_L(z) - P_L^{GL}(z)$. Thus, in principle we can expect significantly different lateral stress profiles when following the IKN procedure with CFD or GLD. This troubling observation places a strong emphasis on the physics

behind force decompositions, particularly for systems with less symmetry such as a bent bilayer or a bilayer with a transmembrane protein where presumably σ^{GL} is not symmetric.

We end this Section by noting that the individual contribution to P_N of all additive components of the potential (e.g. bonds, angles, dihedrals, etc.) are invariant with respect to the method of decomposition. For instance, the contribution of any given dihedral or angle interaction to P_N is the same with CFD or GLD, while the contribution to the lateral stress P_L may drastically depend on the method of decomposition. To understand this fact, recall that for pair potentials (bonds, constraints, van der Waals, and coulomb) both CFD and GLD yield the same contribution to the stress tensor. Then, P_N decomposed with CFD or GLD for the same ensemble takes the form

$$
\begin{aligned}
P_N &= P_{N,m=2} + \sum_M P_{N,m\geq3}^{CFD}, \\
P_N &= P_{N,m=2} + \sum_M P_{N,m\geq3}^{GLD}.
\end{aligned}
\tag{9}
$$

Due to mechanical equilibrium, P_N must be constant and equal to the pressure of the system in both calculations. Therefore, the multibody ($m \geq 3$) potential contributions to P_N must be equal in GFD and CFD in order to balance the pair contributions ($m = 2$). This argument can be extended to each multibody contribution separately, since in the IKN procedure each additive component of the potential can be legitimately decomposed with a different method.

Methods

Local Stress Implementation

Here, we implement a local stress calculation in MD simulations at equilibrium through the Hardy-Murdoch procedure given by Eq. (3). We discretize the simulation volume into a three-dimensional rectangular grid of cell size $\left(a_x, a_y, a_z\right)$, and compute the stress tensor in each node of the grid $x_{(i,j,k)}$. The pointwise contributions are spatially averaged with trilinear weight functions of the

form

$$
w\left(\boldsymbol{x}_{(i,j,k)};\boldsymbol{y}\right) =
\begin{cases}
\prod_I \dfrac{1}{a_I}\left(1 - \dfrac{\left|(\boldsymbol{y} - \boldsymbol{x}_{(i,j,k)})_I\right|}{a_I}\right) & \text{when } \left|(\boldsymbol{y} - \boldsymbol{x}_{(i,j,k)})_I\right| < a_I, \ I = x, y, z \\
0 & \text{otherwise,}
\end{cases}
\tag{10}
$$

which are centered at each $\boldsymbol{x}_{(i,j,k)}$ and whose support is given by the eight grid cells adjacent to it (see Fig. 1 for an illustration in 2D). Common implementations of the Hardy stress in MD simulations use constant weights within each cell,[24,32,51] resulting in noisier and discontinuous stress fields at the edges of the cells. Broader and smoother weight functions such as higher order B-splines or long-range mollifying functions[37,44] produce smoother stress fields, but can excessively smear local features and increase the computational cost. This issue is not minor, since the computational time required to calculate the local stress can be comparable to the time to simulate the system. We also note that the smaller the grid cells are, the longer the MD simulations need to be to adequately sample each local cell. In our experience, the trilinear weighting functions provide a good compromise of smoothness and efficiency. The bond function $B\left(\boldsymbol{x}_{(i,j,k)};\boldsymbol{r}_i^\alpha,\boldsymbol{r}_i^\beta\right)$ can be easily calculated analytically by integrating $w\left(\boldsymbol{x}_{(i,j,k)};\boldsymbol{y}\right)$ along the interaction lines crossing the grid cell.

In addition to the spatial averaging, we must also decompose the forces resulting from multi-body interactions, such as angle and dihedral potentials. In biomolecular simulations, the total potential energy is commonly formulated as an additive decomposition of two-, three- and four-body potentials $V = \sum_a V_{a,2} + \sum_b V_{b,3} + \sum_c V_{c,4}$. As discussed in the Theory section, it is natural to decompose each of these contributions individually, resulting in a unique CFD. Algebraically, the CFD of a $N-$body interaction, $V_{a,N}$ with $N = 3, 4$, can be obtained by solving the overdetermined system of equations

$$
\sum_{\beta=1(\beta \neq \alpha)}^{N} \varphi_{a,N}^{\alpha\beta} \frac{\boldsymbol{r}^{\alpha\beta}}{r^{\alpha\beta}} = -\frac{\partial V_{a,N}}{\partial \boldsymbol{r}^\alpha} = \boldsymbol{F}_{a,N}^\alpha.
\tag{11}
$$

For $N = 3$, there are 3 unknowns $\varphi_{a,N}^{\alpha\beta}$ and 9 equations, see Fig. 2 for an illustration. For $N = 4$, there are 6 unknowns and 12 equations. The existence of the CFD guarantees that this system is
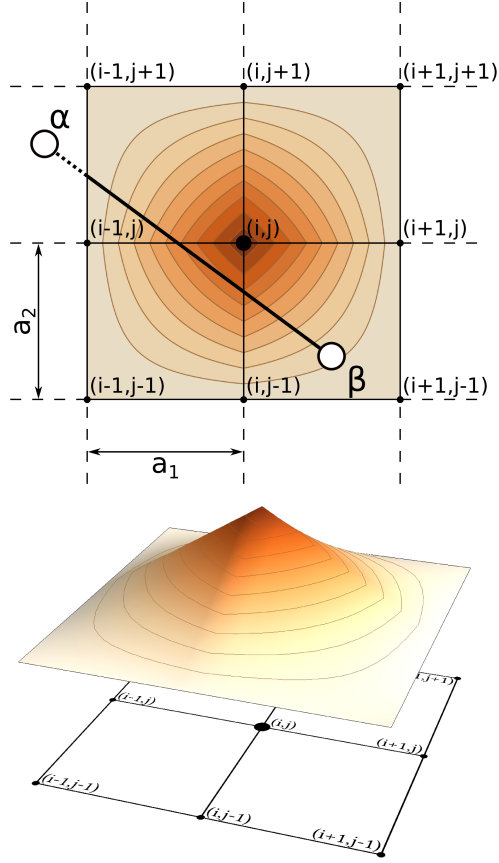
Figure 1. Space discretization into a grid. The pointwise stress tensor is spatially averaged and distributed into regularly spaced grid points with a trilinear weighting function supported on the adjacent cells. The contour plot illustrates the weighting function in 2D. The contribution to the stress tensor at the grid point (i,j) for two interacting particles α and β is weighted by the bond function, $B\left(\boldsymbol{x}_{(i,j)}; \boldsymbol{r}_\alpha, \boldsymbol{r}_\beta\right)$, which is the integral of the weight function, $w\left(\boldsymbol{x}_{(i,j)}, \boldsymbol{y}\right)$, along the line segment connecting α and β. Because of the support of $w\left(\boldsymbol{x}_{(i,j)}, \boldsymbol{y}\right)$, only the solid part of the segment contributes to $B\left(\boldsymbol{x}_{(i,j)}; \boldsymbol{r}_\alpha, \boldsymbol{r}_\beta\right)$.

compatible. The invariance constraints on $V_{a,N}$,

$$\sum_\alpha \boldsymbol{F}_{a,N}^\alpha = \boldsymbol{0}, \qquad \sum_\alpha \boldsymbol{F}_{a,N}^\alpha \times \boldsymbol{r}^\alpha = \boldsymbol{0}, \tag{12}$$

are compatibility equations for solvability of the system. Numerically, the system of equations in Eq. (11) can be solved by generic linear algebra algorithms, such as Gaussian elimination with partial pivoting, or by noting the special form of the equations as implemented in our code.[41] As argued in the Theory section, forces from two-body interactions and from constraints are trivially decomposed into a CFD. Table 1 provides a summary of the types of potentials present in biomolecular simulations and the properties of the CFD.
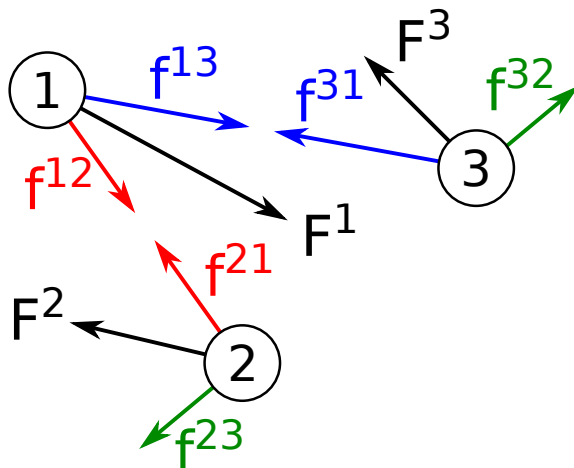
Figure 2. Central force decomposition for a three-body potential. In a multibody interaction such as an angle potential, the net forces, $\boldsymbol{F}^\alpha$, on the interacting particles must be decomposed into pair-wise central forces $\boldsymbol{f}^{\alpha\beta} = \varphi^{\alpha\beta}\hat{\boldsymbol{r}}^{\alpha\beta}$, with $\hat{\boldsymbol{r}}^{\alpha\beta} = \boldsymbol{r}^{\alpha\beta}/r^{\alpha\beta}$. The three unknowns in the CFD, $\varphi^{\alpha\beta}$, can be obtained from the solvable overdetermined linear system $\boldsymbol{F}^1 = \varphi^{12}\hat{\boldsymbol{r}}^{12} + \varphi^{13}\hat{\boldsymbol{r}}^{13}$, $\boldsymbol{F}^2 = -\varphi^{12}\hat{\boldsymbol{r}}^{12} + \varphi^{23}\hat{\boldsymbol{r}}^{23}$, $\boldsymbol{F}^3 = -\varphi^{13}\hat{\boldsymbol{r}}^{13} - \varphi^{23}\hat{\boldsymbol{r}}^{23}$.

As mentioned earlier, the CFD is unique for up to four-body interactions. In fact, this statement holds only when the particles are not collinear ($N = 3$) or coplanar ($N = 4$). In practice, this is not an issue. Most bending and dihedral angle potentials have extrema at 0 and π, and therefore the resulting forces vanish and do not need to be decomposed. This may not be the case for restraining angle potentials, which nevertheless limit the accessible angles away from the pathological angles

Table 1. Number of particles involved in the main MD potentials for biomolecular simulations.

Potential	Particles	Pairwise terms
Coulomb	2	1
Van der Waals	2	1
Angles	3	3
Dihedrals	4	6
Bond constraints	2	1
Harmonic bonds	2	1

under normal simulation conditions.

In addition to the method for local stress calculation described above, which we refer to as *Current implementation (CFD)*, we consider two additional methods. On the one hand, we implement the GLD for three- and four-body potentials instead of the CFD, but stick to our treatment of constraints, which we call *Current implementation (GLD)*. We recall that the theory behind the GLD does not explicitly address constraints, although constraints have been included in previous implementations, along the lines proposed here[32] or with different approaches.[27,38] On the other hand, as a reference to compare our results, we compute stress profiles with a custom version of Gromacs,[42] implementing an algorithm for local stress calculation.[32] This popular implementation, which we refer to as *Reference implementation*, is based on GLD, heuristically decomposes SETTLE constraint forces, and makes reasonable but drastic approximations in the treatment of three- and four-body interactions. Except for SETTLE constraints, bond constraints are treated in the same way in the current and in the reference implementations. We have made publicly available the *Current implementation (CFD and GLD)*[41] as a custom version of the Gromacs software (based on version 4.5.5).

It is worth noting that the SETTLE algorithm aggregates three bond constraints for a water molecule, and outputs the sum of the three constraint forces on each particle, but not the individual Lagrange multipliers. It is easy to recover the three Lagrange multipliers,[48] for instance performing a CFD on the SETTLE forces as if it was a three-body potential. In the current implementation, we adopt this method to identify the Lagrange multipliers of SETTLE constraints both for CFD and GLD, and then follow the standard treatment of constraints described in the Theory Section.

Simulated Systems and Analysis

All atomistic and coarse-grained simulations were conducted with the Gromacs 4.5.5 simulation package[40,52] at the Barcelona Supercomputing Center. Coarse-grained simulations were performed with the unmodified MARTINI[53,54] force-field (FF) and a recently developed FF known as BMW-MARTINI,[55] based on MARTINI and reparametrized for usage with the big multipole water (BMW) model.[56] All coarse-grained simulations are composed of 200 POPE lipids (1-palmitoyl-2-oleoyl-sn-glycero-3-phosphoethanolamine) and 3000 coarse-grained water molecules (equivalent to 12000 atomistic waters). Pressure was semi-isotropically coupled with a Parrinello-Rahman barostat[57] at 1 atm, and the temperature was held constant at 37 °C with a Nosé-Hoover thermostat.[58] MARTINI simulations were performed with a switched Lennard-Jones potential (the switch function is applied at a radius of 0.9 nm and the potential is zero at a radius of 1.2 nm), and a shifted Coulombic potential (cut-off radius of 1.2 nm) with a relative dielectric constant $\epsilon_r = 15$ for explicit screening. The integration time step for this model is 40 fs. The Lennard-Jones interactions for BMW-MARTINI systems were calculated in the same way as MARTINI, except for water-water interactions, where the switch function is applied at a radius of 1.2 nm and the potential is zero at a radius of 1.4 nm. Electrostatic interactions for this model were calculated using a reaction-field treatment[59] with a cut-off radius of 1.4 nm and a dielectric constant $\epsilon_{rf} = 74$. In BMW-MARTINI simulations, the time step was 2 fs for flexible water and 20 fs for rigid water.

Atomistic bilayers were simulated with the Gromos 43A1-S3[60] FF or with the Berger[61] FF obtained from the website of the Tieleman group,[62] with additional modifications for the dihedral angles near double bonds following the work of Bachar et al.[63] For simulations with the G43A1-S3 FF, Lennard-Jones forces where calculated using a twin-range cut-off scheme with interactions within 1.0 nm calculated at every time step and interactions between 1.0 and 1.6 nm only updated every 5 time steps. Lennard-Jones forces for simulations with the Berger FF were calculated with a plain cut-off of 1.0 nm. Long-range electrostatic interactions were computed using the particle-mesh Ewald (PME) method with a real-space cut-off of 1.0 nm and a Fourier grid spacing of 0.15 nm. Pressure was semi-isotropically coupled with a Parrinello-Rahman

barostat at 1 atm, and the temperature was held constant at 37 °C for both POPE and POPC (1-palmitoyl-2-oleoyl-sn-glycero-3-phosphocholine), and at 50 °C for DPPC (1,2-dipalmitoyl-sn-glycero-3-phosphocholine) with a Nosé-Hoover thermostat. All atomistic systems are composed of 200 lipids and 12000 water molecules (SPC/E[64] and SPC[65] for the G43A1-S3 and Berger FF respectively). The integration time step for the atomistic simulations was 2 fs. A summary of all the coarse-grained and atomistic simulated systems is given in Table 2.

All simulated systems except those with the Berger FF were run for a 400 ns equilibration period, followed by a 100 ns data collection period where the positions and velocities were stored every 5 ps. To reduce computational costs, the initial configurations for the systems simulated with the Berger FF were taken from the end of the equilibration period with the G43A1-S3 FF, and re-equilibrated for a 100 ns period followed by 100 ns of data collection. The stored trajectory was then analyzed to produce stress profiles with the *Current implementation (CFD)*, the *Current implementation (GLD)*, and the *Reference implementation (GLD)*. Given that the implementation presented here does not take into account the electrostatic contributions computed in reciprocal space, the analysis for atomistic systems simulated with the PME method was carried out only considering Coulomb forces up to a cut-off radius of 2.2 nm. The accuracy of this common treatment is examined in Appendix A.

Table 2. Summary of simulated systems

System	FF	Lipids	Electrostatics	Water Model	Lipid Bonding	Solvent Bonding	Dihedrals
CG	MARTINI	200 POPE	Reaction-field $r_c = 1.2$ nm	MARTINI	H	-	no
CG-BMW-RW	BMW-MARTINI	200 POPE	Reaction-field $r_c = 1.4$ nm	BMW	H	C	no
CG-BMW-FW	BMW-MARTINI	200 POPE	Reaction-field $r_c = 1.4$ nm	BMW	H	H	no
POPE-PME	G43A1-S3	200 POPE	PME	SPC/E	C	C	yes
POPC-PME	G43A1-S3	200 POPC	PME	SPC/E	C	C	yes
DPPC-PME	G43A1-S3	200 DPPC	PME	SPC/E	C	C	yes
POPC-PMEB	Berger	200 POPC	PME	SPC	C	C	yes
DPPC-PMEB	Berger	200 DPPC	PME	SPC	C	C	yes

H: Harmonic, C: Constraints

17

Results

Effects of Force Decomposition

To test the effect of the force decomposition, either CFD or GLD, and the treatment of bond constraints, we perform local stress calculations on lipid membranes modeled with different interaction potentials. We consider three different coarse-grained models: conventional MARTINI with one-bead water particles[53,54] (CG), reparametrized MARTINI for the big multipole water (BMW) model[55] with rigid bond constraints for water (CG-BMW-RW), and MARTINI-BMW with harmonic bonds for water (CG-BMW-FW). In addition to these coarse-grained models, we also consider the atomistic G43A1-S3[60] model. Although comparison between different atomistic force-fields is beyond the scope of this paper, we include in Appendix B results obtained from simulations of DPPC and POPC simulated with the Berger FF for completeness and easier comparison with previous local stress results. Fig. 3A shows the structure of a coarse-grained POPE lipid with the three types of solvents, and Fig. 3B shows the equivalent atomistic lipid structure.

Figure 3. Representation of the different lipid models considered here. A) CG lipids such as POPE are simulated with harmonic bonds and three different types of water molecules: one bead CG water, BMW water with harmonic bonds, and BMW water with rigid bond constraints. B) Atomistic lipids and water molecules are simulated with rigid bond constraints.

Stress profiles for the coarse-grained and atomistic bilayers calculated with the Current (both with CFD and GLD) and the Reference implementations (see Methods) are shown in Figure 4.
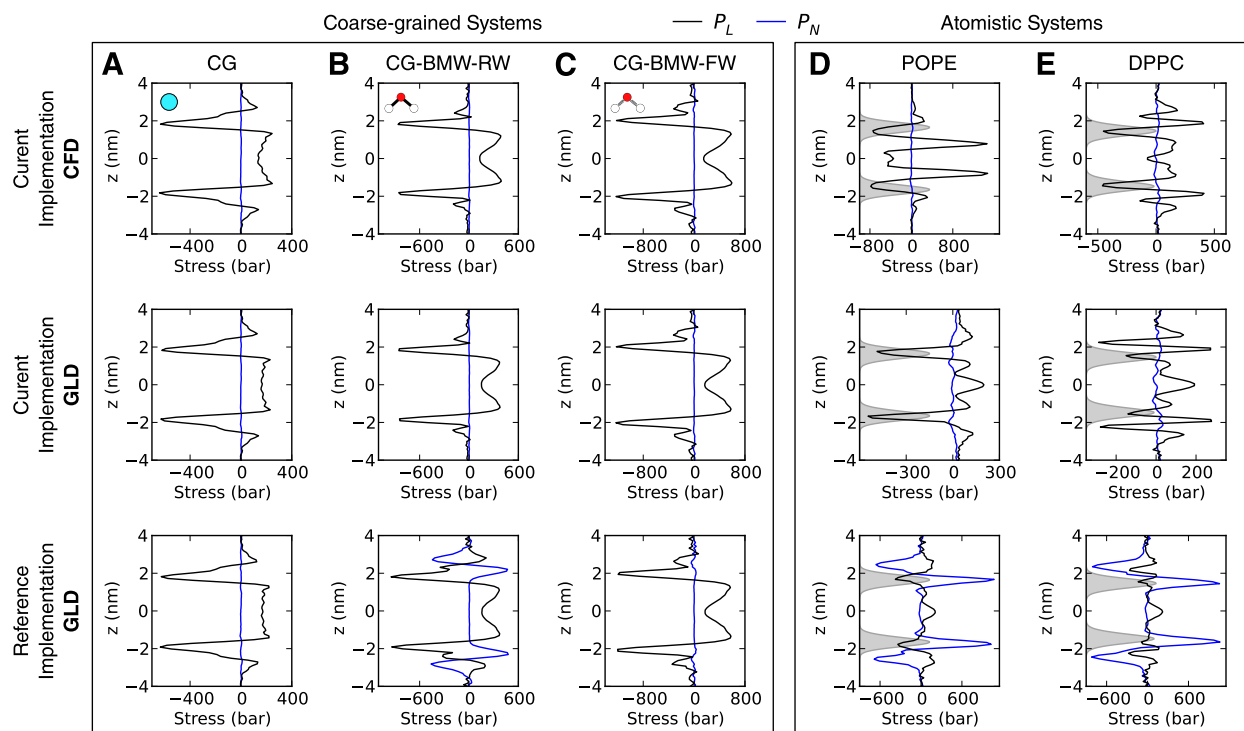
The lateral component of the stress $P_L(z) = -\left(\sigma_{xx} + \sigma_{yy}\right)/2$ is shown in black and the normal component $P_N(z) = -\sigma_{zz}$ is shown in blue. This same color-coding is used in the subsequent figures. In the first model, CG (Fig. 4A), all forces are pairwise central except for those that originate from three-body angle potentials in the lipid tails. Not surprisingly, we only observe minimal variations between CFD and GLD located at the hydrophobic core. As expected from mechanical equilibrium, P_N is constant across the simulation box in all cases.

We move now to a more complex model (BMW-MARTINI) with constraints. In this model, a coarse-grained water molecule (representing 4 real waters) is composed of three charged particles, resembling the structure of real water. Similarly to MARTINI, the bonds in the lipid molecules are treated with harmonic potentials, but the bonds in the BMW coarse-grained water are treated with rigid constraints to improve computational efficiency. Water constraints are usually enforced with the SETTLE[48] algorithm in MD simulations. Fig. 4B shows the stress profiles for the CG-BMW-RW system. As before, the differences between the two flavors of the Current implementation are minimal and located at the hydrophobic core, and with our treatment of constraints P_N is flat. In contrast, the Reference implementation produces a P_N profile with strong unphysical variations at the lipid-water interface, which also distorts the P_L profile in this region, presumably as a result of its heuristic treatment of SETTLE constraints. To confirm this explanation for the spurious P_N profile in the Reference implementation, we analyze a computationally less efficient CG-BMW-FW system with flexible water molecules (Fig. 4C). For this system, the results from the Current and Reference implementations are very similar and show a constant P_N across the simulation box. Note that P_L for the CG-BMW-RW and CG-BMW-FW bilayers (Fig. 4,B and C) are qualitatively very similar, yet because of differences in the compressibility of the systems depending on how water is modeled, the magnitudes of the peaks and their location along z are different.

Atomistic bilayer simulations have two multibody potentials that must be decomposed: angles and dihedrals. Additionally, these models resort to bond constraints both in water and in the lipid molecules, leading to constraint forces that must also be properly treated (see Theory). Stress profiles for the atomistic POPE and DPPC bilayers are shown in Fig. 4,D and E respectively.

19

Figure 4. Importance of the force decomposition. Stress profiles for coarse-grained and atomistic bilayers calculated with the Current (both with CFD and GLD) and the Reference implementations. A) POPE CG bilayer with one-bead coarse-grained water. B) POPE CG-BMW-RW bilayer with BMW water molecules simulated with rigid constraints. C) POPE CG-BMW-FW bilayer with BMW water molecules simulated with harmonic bonds. D) Atomistic POPE bilayer. E) Atomistic DPPC bilayer. The lateral component of the stress $P_L(z) = -\left(\sigma_{xx} + \sigma_{yy}\right)/2$ is shown in black and the normal component $P_N(z) = -\sigma_{zz}$ is shown in blue. The grey-filled curves in the atomistic profiles show the location of the hydrophobic-water interface, identified from the overlap of the density profiles of water and lipid tails, $\rho_{\text{water}}(z) \cdot \rho_{\text{tails}}(z)$, in arbitrary units as a guide to the reader.

These two lipids differ both in the headgroup and tail regions. POPE has one double bond on the 18 carbon chain, and DPPC has two fully saturated chains. Also, in the PE headgroup the nitrogen atom is bonded to three hydrogens, while in PC the nitrogen is bonded to three methyl groups. As before, the Reference implementation applied to atomistic systems produces unphysically large variations in P_N, with magnitudes larger than P_L, near the lipid-water interface as a result of the inadequate treatment of the water constraints. The current implementation corrects this anomaly, both with CFD and GLD. The lateral profiles P_L resulting from the GLD and obtained from the Reference and the Current implementations are quite similar, except for some variations at the lipid-water interface due to constraints. In contrast, the Current implementation with CFD exhibits remarkably different P_L profiles for both POPE and DPPC, in terms of the magnitude and location of the peaks across the bilayer. One of the most striking features of the CFD lateral profile for POPE, absent in the GLD counterpart, is the presence of large positive peaks in the middle of each leaflet, which are ten times larger in magnitude than the positive peaks in the hydrophobic core of DPPC. The lateral profile in the DPPC bilayer analyzed with CFD and GLD significantly differ in the lipid-water interface and in the hydrophobic core. These dramatic differences in P_L should be attributed to the decomposition of multibody potentials.

Individual Contributions to the Stress

To further investigate the nature of the stress profiles and focusing on the CFD, we separate the kinetic and potential contributions for the coarse-grained (CG and CG-BMW-RW) and atomistic models of POPE, as shown in Fig. 5. Thermodynamic equilibrium in these models arises from the sum of various contributions and therefore it is expected that the partial stress profiles of each individual interaction may not display similar behavior when compared across models, e.g. atomistic simulations include potentials that are not considered in the CG systems and change the equilibrium conditions. The treatment of water in the three models is one of the biggest factors influencing the behavior of the individual contributions to the stress.

We first focus on the CG model, which contains the least number of interaction potentials

(Fig. 5A). We check that for this unconstrained system, the kinetic part of the stress locally satisfies the equipartition theorem and therefore $P_L^K(z) = P_N^K(z) = \rho(z)k_BT$, where $\rho(z)$ is the particle density profile. The water beads in the CG model are not charged and therefore cannot reproduce the entropic or enthalpic behavior of real water, which are at the origin of the hydrophobic effect keeping the bilayer in place. This makes it necessary to include attractive van der Waals interactions at the lipid headgroups and in the water beads to preserve the integrity of the bilayer and the cohesion of fluid water. Therefore, van der Waals forces result in negative values in both P_L and P_N. The lipid headgroups also present electrostatic interactions that lead to net cohesive stresses in this region. The angle contribution presents a repulsive component in P_N and an attractive component in P_L, which result from the vertical orientation of the lipids as well as from their packing within the membrane. The bonding contribution to both P_L and P_N is positive due to the reduction, on average, of bond lengths within the packed lipids.

In the more sophisticated CG-BMW-RW (Fig. 5B), the different water treatment introduces major changes in several partial profiles when compared to the CG model. These changes are located in the bulk water and at the lipid-water interface, since the two models are very similar in the hydrophobic core. As expected, the kinetic contribution increases with the degrees of freedom in water. The Coulomb interactions between water molecules, which result in cohesive intermolecular forces due to the dipole-dipole interactions, completely changes the role of van der Waals forces. In this model, van der Waals forces in water mostly result in collisions that generate high repulsive stresses. On the other hand, the SETTLE constraints provide the intramolecular forces that keep the water structure fixed, resulting in cohesive stresses. At the lipid-water interphase, where the particle density is highest in the bilayer, the bond contribution presents an attractive stress to compensate for the higher rate of van der Waals collisions.

The individual contributions in the atomistic system (Fig. 5C) are qualitatively similar to those in the CG-BMW-RW model due to the analogous treatment of water, although the stress magnitudes are significantly different. Bonding forces, which are treated with LINCS constraints in this model, result in both attractive and repulsive stresses in the headgroup region. The positive

22

peaks stem from the repulsive constraint forces that balance the attractive electrostatic interaction between the phosphate and ethanolamine groups. The CG and CG-BMW-RW models do not present this feature as these two charged groups are directly connected by a bond and therefore the electrostatic force is excluded.
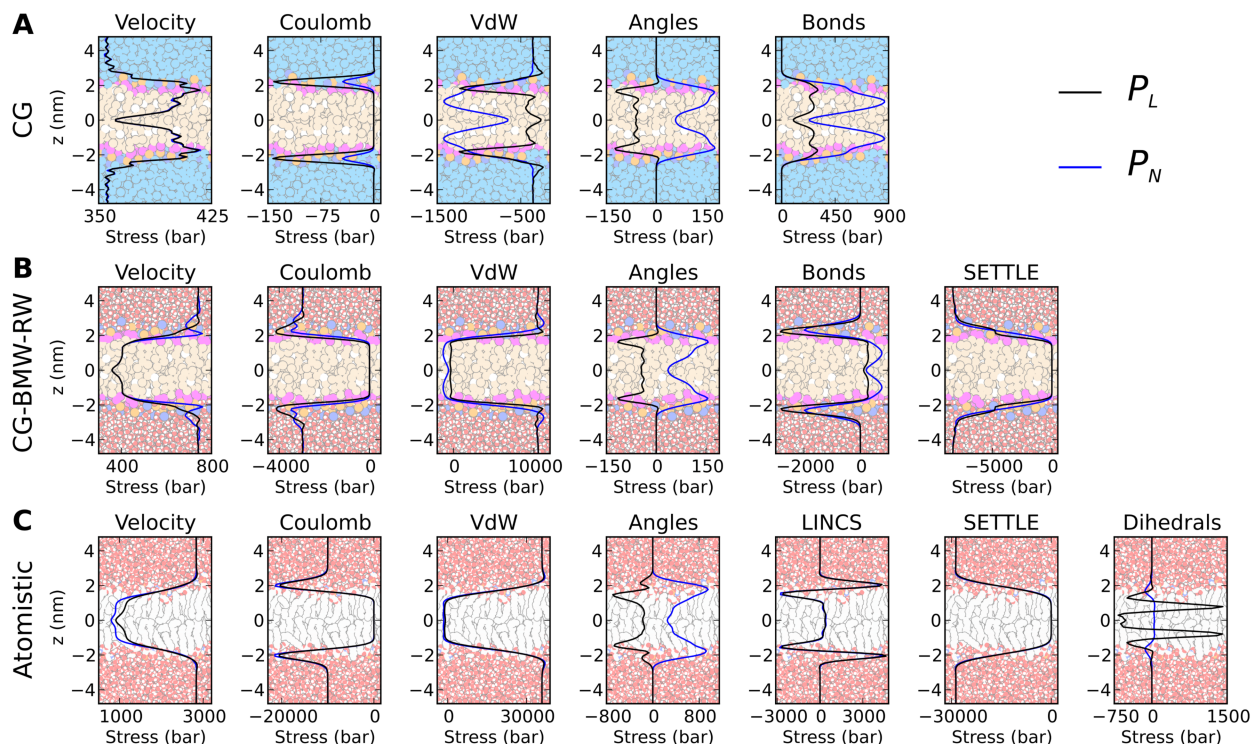
Figure 5. Individual contributions to the total stress of coarse-grained and atomistic membrane simulations. The lateral profile P_L is represented by black curves, while P_N is plotted in blue. The translucent image in the background of each plot depicts the lipid bilayer (tanned/grey atoms) and the water (light blue/red atoms) regions to guide the reader. (A) shows the contributions for the MARTINI CG POPE system, (B) shows those of the BMW-MARTINI (CG-BMW-RW) POPE with rigid water (SETTLE), and (C) shows the contributions of the atomistic POPE-PME with rigid lipid (LINCS) and water (SETTLE) bonds. While this last system was simulated with long-range PME electrostatics, the Coulomb contribution to the stress for this system was computed using a plain cut-off with a radius of 2.2 nm (see Methods).

Critical role of dihedral contributions to the stress profile

In the atomistic model of POPE, the dihedral contributions to P_L displays large positive and negative values as shown in Fig. 5C (rightmost panel). In fact, as emphasized in Fig. 6A, this dihedral contribution nearly coincides with the total lateral stress profile within the hydrophobic core, and

23

therefore the other contributions nearly balance each other in this region. As suggested by the excellent correlation between the location of the double bond and the large positive peaks in each leaflet of POPE, see Fig. 6A, we attribute this feature of the lateral stress profile to the dihedral potential that restraints the planar geometry of this *cis* double bond. The potentials used to restrain the geometry of a double bond are significantly stiffer compared to other dihedral interactions. We present a similar comparison of the dihedral contribution vs the total lateral profile for POPC, see Fig. 6B, differing from POPE in the headgroup but also exhibiting a double bond in the tails. Again, the contribution of dihedral forces overwhelmingly dominates the P_L profile in the hydrophobic core. We compare this system with DPPC, see Fig. 6C, which differs from POPC in that it does not have double bonds. This system shows much smaller positive peaks in the hydrophobic core, and the total pressure profile does not closely follow the dihedral contribution, which is nevertheless significant. Comparison of Fig. 6B and C suggests that double bonds in the lipid tails strongly affect the way stresses are distributed across the bilayer. This is consistent with experimental observations showing that the bending elasticity modulus of a fluid bilayer decreases with the number of unsaturations in the lipid tails, while the lateral area compressibility practically remains unchanged.[66,67] The GLD does not capture the effect of double bonds in P_L, see Fig. 4D, and therefore misses the strong mechanical effect of dihedrals in the hydrophobic core predicted by CFD stress calculations. Also, note that the P_L obtained by the CFD results in reduced or negative stresses in the bilayer midplane, consistent with the reduced density of the system here, while the GLD P_L shows increased stresses for atomistic models of both POPE and DPPC (Fig. 4, D and E) in this region.

While the effects of the lipid unsaturations clearly dominate the stress profile differences between these systems, there are also smaller variations in the headgroup region. In all three systems shown in Fig. 6, there is a clear correlation between the large negative peak and the hydrophobic-water interface as expected from their unfavorable interaction, which induces a cohesive stress to minimize the exposure of the lipid tails to the water. In the headgroup region, the repulsion between the charged atoms (e.g. phosphorous, see cyan density plots in Fig. 6) results in a positive

peak.
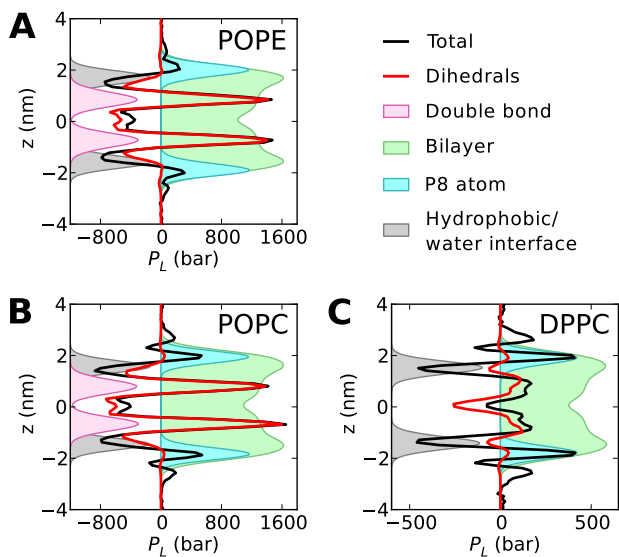
Figure 6. Dihedral contribution to the lateral stress profile P_L (red curves) compared to the total P_L profile (black curves), in atomistic POPE (A), POPC (B), and DPPC (C) bilayers. Density plots (filled areas, in arbitrary units) of particular lipid components are included for reference. The hydrophobic-water interface is identified from the overlap of water and lipid tail densities, $\rho_{\text{water}}(z) \cdot \rho_{\text{tails}}(z)$.

Summary and discussion

We have presented an implementation of the local stress calculation from MD simulations of atomistic and coarse-grained biomembranes that consistently treats constraints, and made it publicly available.[41] As a result of our treatment of bond constraints and in contrast with previous implementations, we obtain flat profiles of the stress normal to the membrane as required in equilibrium, both for atomistic and coarse-grained systems. Furthermore, the lateral pressure profile obtained with the current implementation is devoid of artifacts at the lipid-water interface associated with an improper treatment of constraints. By implementing two different force decompositions of multibody interactions in an Irving and Kirkwood procedure,[9] one based on the central force decomposition (CFD)[15,37] and a another one proposed by Goetz and Lipowsky (GLD),[14] we highlight the ambiguity of lateral stress profiles, which are routinely used to understand bilayer mechanics

and to parametrize coarse-grained force fields. We find that CFD and GLD lead to very different lateral stress profiles in atomistic models, and favor the CFD, which produces symmetric stresses by construction and can be seen as a canonical decomposition for potentials with up to four-body interactions such as those used in biomolecular simulations. The CFD lateral stress profiles are very sensitive to the bilayer chemical composition (POPE, POPC, or DPPC), and are strongly determined by dihedral interactions, which become critical in the presence of double bonds as suggested by experimental data.

We find that coarse-grained models with simplified water treatments produce individual stress contributions very different from those obtained from atomistic models. Coarse-grained systems with more realistic water models more closely mimic the atomistic system, although they ignore important effects due for instance to double bonds, and underestimate the magnitude of the stresses. Detailed stress calculations such as those presented here may help parametrize coarse-grained force fields, or suggest consistent methods to rescale coarse-grained stress profiles for quantitative estimations.

The unsettling subjectivity of lateral stress profiles in bilayer membranes calls for a close examination of the physical grounds of different force decompositions for multibody potentials,[15] although the automatic symmetry of stresses based on CFD is a solid argument in favor of it. Lateral stress profiles stemming from different force decompositions may be tested against global observables. For instance, elastic properties computed from continuum fields should agree with their global thermodynamic evaluation, although in practice such comparisons are challenging and have not been satisfying.[68] The chemical specificity of the CFD stress profiles, particularly the strong role of double bonds in the oleoyl chain, suggests a more systematic exploration with MD of the relationship between the chemical structure of lipids and the mechanical bilayer properties, that may be compared with the experimental record. We are currently applying the methodology introduced here to quantitatively understand the influence of sterols in the mechanical behavior of bilayer membranes.

26

Appendix A - Contributions from long range electrostatic interactions

The electrostatic contributions to the stress from systems simulated with long-range PME (or other reciprocal space method) is only approximately calculated as our implementation does not include these forces currently. A common method for including reciprocal space electrostatic interactions is by means of the Harasima contour[69] as detailed by Sonne et al.[25] However, this method divides the simulation box into slabs (spanning the membrane plane), where the total long-range electrostatic contributions are calculated. As such, the Harasima contour method only computes stress profiles and not the 3D tensor over the simulation volume. Furthermore, it is not clear whether this method is compatible with the CFD stress calculation formulated by Admal and Tadmor.[15] It may be possible in a future version of our implementation to include PME contributions into the local stress calculation following the work of Hatch et al.[70]

For systems simulated with PME, we follow the usual procedure and compute the stress including only electrostatic forces up to a given cut-off radius. To investigate the effect of this approximation, we examine the dependence of the stress profile of the atomistic POPE-PME system with respect to the cut-off radius, see Fig. 7. We observe that the stress profiles show little

difference beyond a cut-off of 2.2 nm, after which the computational cost increases very rapidly. A very stringent test of convergence of the stress profiles with respect to cut-off radius is to integrate the local stresses and compare the resultant quantity with the overall system pressure controlled by the barostat, which should coincide if electrostatic forces were consistently treated. We find that the integrated overall system pressure converges very slowly to 1 bar. These tests support using a cut-off of 2.2 nm to compute the electrostatic components of the stress profiles, as done in the manuscript, but also suggest the need for a self-consistent treatment for accurate estimation of global properties from stress profiles.
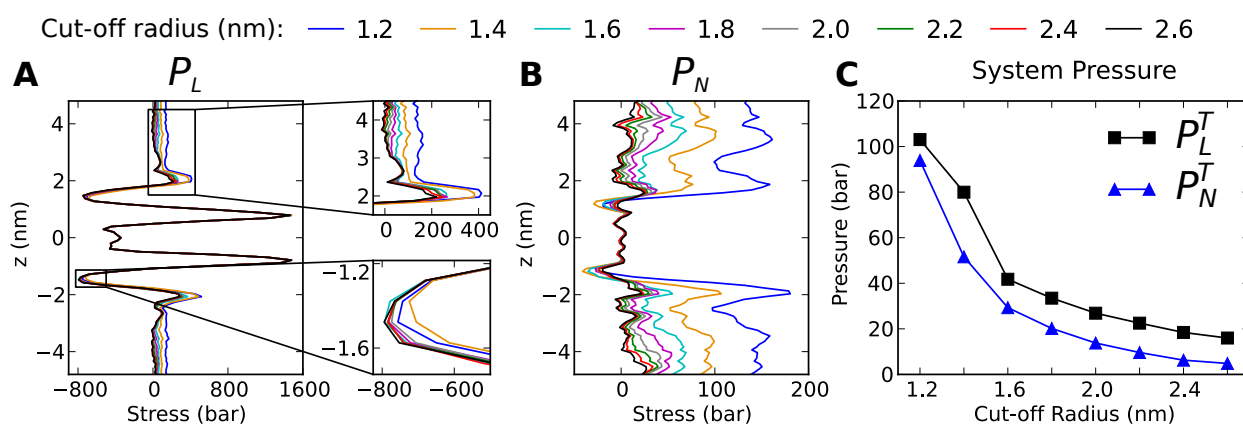

Figure 7. Effect of cut-off in the electrostatic contribution to the stress profiles for a POPE bilayer simulated with long-range PME contributions. Given that the forces from PME are not included consistently in the present implementation of the local stress calculation, only Coulomb interactions up to a given radius contribute to the analysis. The figure shows the dependence on the plain cut-off radius (1.2-2.6 nm) of P_L (A), P_N (B), and the overall system pressure (C).

Appendix B - Stress profiles for lipids simulated with the Berger force-field

Although there are many available force-fields for the simulations of lipid bilayers, a large number of previous works have used the so-called Berger FF. For completeness and easier comparison of our local stress implementation, we include stress profiles of POPC (Fig. 8, A and B) and DPPC (Fig. 8, C and D) membranes simulated with the Berger FF and analyzed with both CFD and GLD.

The harmonic potential used to restrain the double bond dihedral in the Berger FF (as parametrized in the GROMOS87 FF[71]) has a significantly softer well compared to the periodic potential used in the G43A1-S3 (as parametrized by Smith and Paul[72]), and therefore the positive peaks in the middle of each leaflet of POPC, when using CFD (Fig. 8A), in the Berger FF are much smaller compared to those seen in the G43A1-S3 FF (Fig. 6B). The CFD results for DPPC are qualitatively very similar for the Berger (Fig. 8C) and G43A1-S3 FF (Fig. 6).
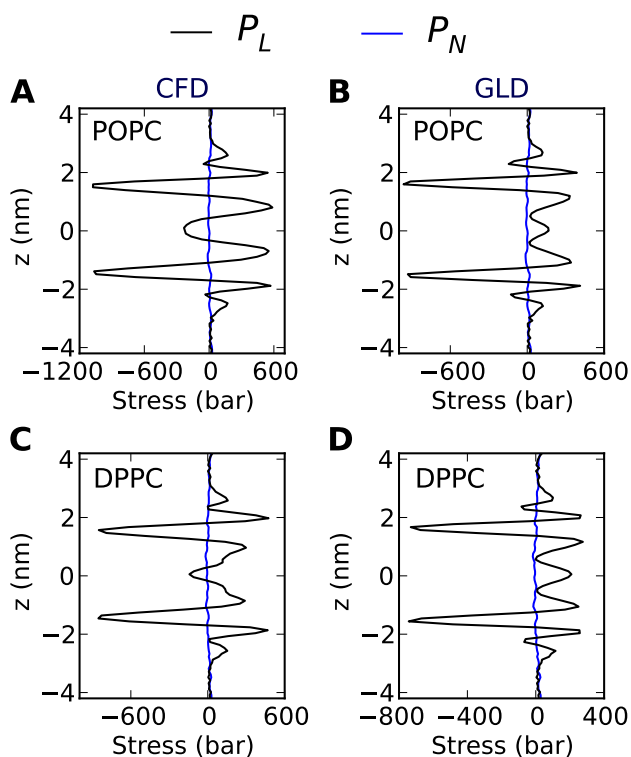
Figure 8. Stress profiles (P_L in black and P_N in blue) of POPC (A and B) and DPPC (C and D) membranes simulated with the Berger FF (see Methods) and analyzed with both CFD (A and C) and GLD (B and D).

References

(1) Hannun, Y. a.; Obeid, L. M. *Nat. Rev. Mol. Cell Bio.* **2008**, *9*, 139–150.

(2) Musille, P. M.; Kohn, J. a.; Ortlund, E. a. *FEBS lett.* **2013**, *587*, 1238–1246.

(3) Michell, R. H. *Nat. Rev. Mol. Cell Bio.* **2008**, *9*, 151–161.

(4) Dumas, F.; Tocanne, J. F.; Leblanc, G.; Lebrun, M. C. *Biochemistry-US* **2000**, *39*, 4846–4854.

(5) McMahon, H. T.; Gallop, J. L. *Nature* **2005**, *438*, 590–596.

(6) Botelho, A. V.; Huber, T.; Sakmar, T. P.; Brown, M. F. *Biophys. J.* **2006**, *91*, 4464–4477.

(7) Marsh, D. *Biophys. J.* **2008**, *94*, 3996–4013.

(8) Phillips, R.; Ursell, T.; Wiggins, P.; Sens, P. *Nature* **2009**, *459*, 379–385.

(9) Irving, J. H.; Kirkwood, J. G. *J. Chem. Phys.* **1950**, *18*, 817–829.

(10) Noll, W. *J. Natural Mech. and Anal.* **1955**, *4*, 627–646.

(11) Hardy, R. J. *J. Chem. Phys.* **1982**, *76*, 622–628.

(12) Murdoch, A. I. *Q. J. Mech. Appl. Math.* **1983**, *36*, 163–187.

(13) Schofield, P.; Henderson, J. *Proc. R. Soc. Lond. A* **1982**, *379*, 231–246.

(14) Goetz, R.; Lipowsky, R. *J. Chem. Phys.* **1998**, *108*, 7397–7409.

(15) Admal, N. C.; Tadmor, E. B. *J. Elast.* **2010**, *100*, 63–143.

(16) Marsh, D. *Biophys. J.* **2007**, *93*, 3884–3899.

(17) Cantor, R. S. *Biochemistry-US* **1997**, *36*, 2339–2344.

(18) Marrink, S. J.; Risselada, H. J.; Yefimov, S.; Tieleman, D. P.; de Vries, A. H. *J. Phys. Chem. B* **2007**, *111*, 7812–7824.

(19) Sodt, A. J.; Head-Gordon, T. *J. Chem. Phys.* **2010**, *132*, 205103–205111.

(20) Orsi, M.; Michel, J.; Essex, J. W. *J. Phys.: Condens. Matter* **2010**, *22*, 155106–155121.

(21) Kamo, T.; Nakano, M.; Kuroda, Y.; Handa, T. *J. Phys. Chem. B* **2006**, *110*, 24987–24992.

(22) Templer, R. H.; Castle, S. J.; Curran, A. R.; Rumbles, G.; Klug, D. R. *Faraday Discuss.* **1998**, *111*, 41–53.

(23) Lindahl, E.; Edholm, O. *J. Chem. Phys.* **2000**, *113*, 3882–3893.

(24) Gullingsrud, J.; Schulten, K. *Biophys. J.* **2004**, *86*, 3496–3509.

(25) Sonne, J.; Hansen, F. Y.; Peters, G. H. *J. Chem. Phys.* **2005**, *122*, 124903–124912.

(26) Vanegas, J. M.; Longo, M. L.; Faller, R. *J. Am. Chem. Soc.* **2011**, *133*, 3720–3723.

(27) Yoo, J.; Cui, Q. *Biophys. J.* **2013**, *104*, 117–127.

(28) Patra, M. *Eur. Biophys. J.* **2005**, *35*, 79–88.

(29) Ngo, V. A.; Kalia, R. K.; Nakano, A.; Vashishta, P. *J. Phys. Chem. B* **2012**, *116*, 13416–13423.

(30) Baoukina, S.; Marrink, S. J.; Tieleman, D. P. *Faraday Discuss.* **2010**, *144*, 393–409.

(31) Ollila, O. H. S.; Louhivuori, M.; Marrink, S. J.; Vattulainen, I. *Biophys. J.* **2011**, *100*, 1651–1659.

(32) Ollila, O. H. S.; Risselada, H.; Louhivuori, M.; Lindahl, E.; Vattulainen, I.; Marrink, S. *Phys. Rev. Lett.* **2009**, *102*, 1–4.

(33) Ollila, O. S. Lateral pressure profile calculations of lipid membranes from atomic scale molecular dynamics simulations. M.Sc. thesis, Helsinki University of Technology, 2006.

(34) Ollila, O. S. Lateral pressure in lipid membranes and its role in function of membrane proteins. Ph.D. thesis, Tampere University of Technology, 2010.

(35) *Faraday Discuss.* **2013**, *161*, 301.

(36) Orsi, M.; Essex, J. W. *Faraday Discuss.* **2013**, *161*, 249–272.

(37) Tadmor, E. B.; Miller, R. E. *Modeling Materials: Continuum, Atomistic and Multiscale Techniques*; Cambridge University Press, 2011.

(38) Kasson, P. M.; Hess, B.; Lindahl, E. *Chem. Phys. Lipids* **2013**, *169*, 106 – 112.

(39) Hartmann, C.; Schutte, C.; Ciccotti, G. *J. Chem. Phys.* **2010**, *132*, 111103.

(40) Pronk, S.; Páll, S.; Schulz, R.; Larsson, P.; Bjelkmar, P.; Apostolov, R.; Shirts, M. R.; Smith, J. C.; Kasson, P. M.; van der Spoel, D.; Hess, B.; Lindahl, E. *Bioinformatics* **2013**, *29*, 845–854.

(41) Vanegas, J. M.; Torres-Sánchez, A.; Arroyo, M. Computing the Local Stress Tensor in MD Simulations. `http://www.lacan.upc.edu/LocalStressFromMD`.

(42) Marrink, S. J. 3D pressure field. `http://md.chem.rug.nl/cgmartini/index.php/3d`.

(43) Hardy, R.; Root, S.; Swanson, D. *AIP Conf. Proc.* **2002**, 7–10.

(44) Murdoch, A. I. *J. Elast.* **2007**, *88*, 113–140.

(45) Murdoch, A. I. *J. Elast.* **2003**, *71*, 105–131.

(46) Hess, B.; Bekker, H.; Berendsen, H. J. C.; Fraaije, J. G. E. M. *J. Comput. Chem.* **1997**, *18*, 1463–1472.

(47) Forester, T. R.; Smith, W. *J. Comput. Chem.* **1998**, *19*, 102–111.

(48) Miyamoto, S.; Kollman, P. A. *J. Comput. Chem.* **1992**, *13*, 952–962.

(49) Jakobsen, A. F.; Mouritsen, O. G.; Besold, G. *J. Chem. Phys.* **2005**, *122*, 204901.

(50) Varnik, F.; Baschnagel, J.; Binder, K. *J. Chem. Phys.* **2000**, *113*, 4444–4453.

(51) Yoo, J.; Cui, Q. *Biophys. J.* **2009**, *97*, 2267–2276.

(52) Hess, B.; Kutzner, C.; van Der Spoel, D.; Lindahl, E. *J. Chem. Theory Comput.* **2008**, *4*, 435–447.

(53) Marrink, S. J.; de Vries, A. H.; Mark, A. E. *J. Phys. Chem. B* **2004**, *108*, 750–760.

(54) Marrink, S. J.; Risselada, H. J.; Yefimov, S.; Tieleman, D. P.; de Vries, A. H. *J. Phys. Chem. B* **2007**, *111*, 7812–7824.

(55) Wu, Z.; Cui, Q.; Yethiraj, A. *J. Chem. Theory Comput.* **2011**, 3793–3802.

(56) Wu, Z.; Cui, Q.; Yethiraj, A. *J. Phys. Chem. B* **2010**, *114*, 10524–10529.

(57) Parrinello, M.; Rahman, A. *J. Appl. Phys.* **1981**, *52*, 7182–7190.

(58) Evans, D. J.; Holian, B. L. *J. Chem. Phys.* **1985**, *83*, 4069–4074.

(59) Tironi, I. G.; Sperb, R.; Smith, P. E.; van Gunsteren, W. F. *J. Chem. Phys.* **1995**, *102*, 5451–5459.

(60) Chiu, S.-W.; Pandit, S. A.; Scott, H. L.; Jakobsson, E. *J. Phys. Chem. B* **2009**, *113*, 2748–2763.

(61) Berger, O.; Edholm, O.; Jähnig, F. *Biophys. J.* **1997**, *72*, 2002–2013.

(62) Tieleman, D. P. Structures and Topologies. `http://wcm.ucalgary.ca/tieleman/downloads`.

(63) Bachar, M.; Brunelle, P.; Tieleman, D. P.; Rauk, A. *J. Phys. Chem. B* **2004**, *108*, 7170–7179.

(64) Berendsen, H. J. C.; Grigera, J. R.; Straatsma, T. P. *J. Phys. Chem.* **1987**, *91*, 6269–6271.

(65) Berendsen, H. J. C.; Postma, J. P. M.; van Gunsteren, W. F. In *Intermolecular Forces*; Pullman, B., Ed.; Reidel: Dordrecht, 1981; pp 331–342.

(66) Rawicz, W.; Olbrich, K.; McIntosh, T. *Biophys. J.* **2000**, *79*, 328–339.

(67) Marsh, D. *Chem. Phys. Lipids* **2006**, *144*, 146–159.

(68) Hu, M.; de Jong, D. H.; Marrink, S. J.; Deserno, M. *Faraday Discuss.* **2013**, *161*, 365–382.

(69) Harasima, A. *Adv. Chem. Phys.* **1958**, *1*, 203–237.

(70) Hatch, H. W.; Debenedetti, P. G. *J. Chem. Phys.* **2012**, *137*, 035103.

(71) van Gunsteren, W. F.; Berendsen, H. J. C. *Groningen Molecular Simulation (GROMOS) Library Manual*; BIOMOS: Groningen, The Netherlands, 1987; pp 1–221.

(72) Smith, G.; Paul, W. *J. Phys. Chem. A* **1998**, *102*, 1200–1208.
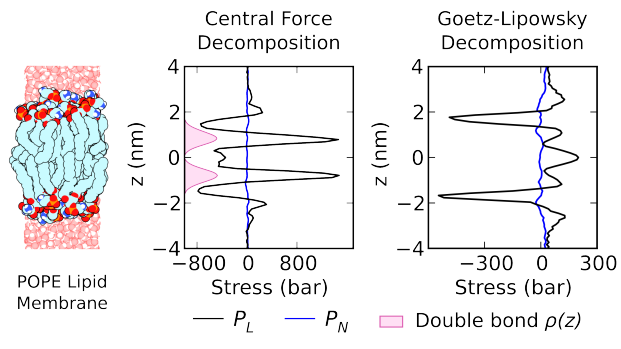
Figure 9. For table of contents only.